NASA/TM-20260006171

Near Real-Time Thermospheric Density Monitoring from Public Satellite Tracking and Space Weather Data

Daniel J. Gershman
NASA Goddard Space Flight Center, Greenbelt, MD

July 2026

NASA STI Program Report Series

Since its founding, NASA has been dedicated to the advancement of aeronautics and space science. The NASA scientific and technical information (STI) program plays a key part in helping NASA maintain this important role.

The NASA STI program operates under the auspices of the Agency Chief Information Officer. It collects, organizes, provides for archiving, and disseminates NASA's STI. The NASA STI program provides access to the NTRS Registered and its public interface, the NASA Technical Reports Server, thus providing one of the largest collections of aeronautical and space science STI in the world. Results are published in both non-NASA channels and by NASA in the NASA STI Report Series, which includes the following report types:

- TECHNICAL PUBLICATION. Reports of completed research or a major significant phase of research that present the results of NASA Programs and include extensive data or theoretical analysis. Includes compilations of significant scientific and technical data and information deemed to be of continuing reference value. NASA counterpart of peer-reviewed formal professional papers but has less stringent limitations on manuscript length and extent of graphic presentations.

- TECHNICAL MEMORANDUM. Scientific and technical findings that are preliminary or of specialized interest, e.g., quick release reports, working papers, and bibliographies that contain minimal annotation. Does not contain extensive analysis.

- CONTRACTOR REPORT. Scientific and technical findings by NASA-sponsored contractors and grantees.

- CONFERENCE PUBLICATION. Collected papers from scientific and technical conferences, symposia, seminars, or other meetings sponsored or co-sponsored by NASA.

- SPECIAL PUBLICATION. Scientific, technical, or historical information from NASA programs, projects, and missions, often concerned with subjects having substantial public interest.

- TECHNICAL TRANSLATION. English-language translations of foreign scientific and technical material pertinent to NASA's mission.

Specialized services also include organizing and publishing research results, distributing specialized research announcements and feeds, providing information desk and personal search support, and enabling data exchange services.

For more information about the NASA STI program, see the following:

- Access the NASA STI program home page at http://www.sti.nasa.gov

.

NASA/TM-20260006171

Near Real-Time Thermospheric Density Monitoring from Public Satellite Tracking and Space Weather Data

Daniel J. Gershman
NASA Goddard Space Flight Center, Greenbelt, MD

National Aeronautics and
Space Administration

NASA Goddard Space Flight Center
Greenbelt, MD

July 2026

Artificial Intelligence (AI) Usage Disclosure
This document was created with assistance from Claude (Anthropic, claude.ai) for manuscript editing, code execution, and data processing. The content has been reviewed and edited by Daniel J. Gershman. More information on the extent and nature of AI usage is included in the Acknowledgements sections of the document.

Available from:

NASA STI Program / Mail Stop 050
NASA Langley Research Center
Hampton, VA 23681-2199

Abstract. We present a framework to achieve near real-time (NRT) monitoring of the Low Earth Orbit (LEO) environment using publicly available data. We first assimilate Two-Line-Elements (TLEs) from thousands of ballistically stable LEO objects to parameterize the shape and scale of the global atmosphere from the past ~24 hours. When compared to available reference data from 2014 to 2026, our estimates are shown to have an accuracy of ~10-20% for altitudes between 200km and 600km during even the most extreme geomagnetic storms. We then parameterize variations in mass density using solar and geomagnetic activity indices, enabling extension of the TLE-derived solution through short-term forecasts. Our approach enables actionable nowcasts and forecasts of the upper atmosphere for the broader LEO community.

1. Introduction

Drag acceleration forces acting on objects in Low Earth Orbit (LEO) by the upper atmosphere lead to orbital decay. As a growing number of satellites are launched into space, the need for accurate tracking and orbital prediction becomes increasingly critical [*GAO Report GAO-22-105166,* 2022]. Orbit propagation is complicated by the dynamic response of the upper atmosphere [*Oliveira and Zesta,* 2019]. When the upper atmosphere is heated, the density in LEO orbits increases. Depending on the energy source, global increases in satellite drag can vary slowly over weeks or as rapidly as a few hours [*Zesta and Oliveira,* 2019; *Oliveira et al.* 2025]. Uncertainties in the upper atmospheric state lead to uncertainties in object orbit determination, which in turn lead to increased complexity in collision avoidance, station-keeping, and tracking [*Burke,* 2018; *Thayer et al.* 2021; *Berger et al.* 2023; *Bruinsma et al.* 2023a].

There are a number of currently available models that enable forecasts of the atmospheric state, varying from physics based (e.g., WAM-IPE [*Akmaev,* 2011; *Maruyama et al.* 2016], GITM [*Ridley et al.* 2006]), fully empirical (e.g., JB2008 [*Bowman et al.* 2008], NRLMSISE-00 [*Picone et al.,* 2002], NRLMSIS2.0 [*Emmert et al.,* 2021a], MSIS-UQ [*Licata et al.* 2022]) to semi-empirical (e.g., DTM 2020 [*Bruinsma and Boniface,* 2021]) and data-assimilation scaled empirical (e.g, HASDM [*Storz et al.* 2005]). Models that do not incorporate near real-time data assimilation to anchor the density suffer from significant systematic uncertainties during geomagnetic storms [*Kalafatoglu Eyiguler et al.,* 2019; *Bruinsma et al.,* 2021; *Bruinsma and Laurens,* 2024; *Wang et al.,* 2026], limiting operational applications. Most of these models provide the full atmospheric spatial structure as functions of latitude and longitude and altitude. While spatial structure (latitude, longitude, local time) can modulate individual satellite drag, globally-averaged altitude profiles nonetheless provide actionable insights for operations focused on orbit-average or multi-day impacts of orbital decay.

The current standard for operational quality is the HASDM model [*Storz et al.* 2005], which assimilates proprietary tracking data from the U.S. Space Force for a set of calibration satellites into a thermospheric model. Originally HASDM was built around the J70 empirical model [*Jacchia,* 1970] and now scales JB2008 [*Bowman et al.* 2008]. Operational application of HASDM is highly restricted, with only archival data available for public scientific use. Alternatively, Two-Line-Element (TLE) tracking data [*Vallado et al.* 2006] are publicly available and updated several times per day by U.S. Space Force (via Space-Track.org) for all NORAD-tracked objects. These TLEs are produced by fitting tracking observations through the SGP4 orbital propagator model with estimated accuracies around the element epoch to be on the order of ~1-3km [*Vallado et al.,* 2006]. While TLE data are inherently noisier than precise tracking of HASDM, the sheer quantity of data can be used to reduce noise, assuming objects that are experiencing free orbital decay can be clearly identified from the broader TLE database. TLEs have previously been used to derive historical models of the atmosphere (e.g., TLE2021 [*Emmert et al.* 2021b]) comparable with HASDM at the daily-mean level [*Bruinsma et al.* 2023b], but not designed for NRT applications. The release latency between TLE observation epoch and public availability is typically several hours (up to ~24 h), fundamentally limiting their direct real-time use.

However, proxies for the energy sources that drive the upper atmospheric state are available in NRT. These data are comprised of solar and geomagnetic activity indices corresponding to the heating of the upper atmosphere by solar EUV and auroral zone particle precipitation, Poynting flux, and Joule heating. Indices such as F10.7, E10.7, ap, Kp, and Dst are used as inputs into empirical models to predict atmospheric density profiles. The impact of each energy source on the state of the upper atmosphere is highly complex and non-linear, exhibiting significant seasonal and solar cycle variations [*Emmert,* 2015; *Emmert et al.,* 2021b; *Bowman et al.,* 2008]. However, the average response of the upper atmosphere is fairly linear with energy input on shorter time scales (i.e., weeks), especially when considering the orbit-averaged drag acceleration experienced by an individual satellite [*Gershman,* 2026a,b]. *Parker and Linares* [2026] also demonstrated a direct relationship between energy inputs and drag acceleration experienced by a given object in LEO without the need for a fine-structured global atmospheric model. A well-established parameterization of atmospheric mass density in terms of energy inputs will remain valid for several days, enabling extrapolation of the global atmospheric state from a solid anchor point [*Gershman,* 2026a].

Here we develop a process for enabling NRT monitoring of the upper atmosphere. First, in section 2, we present a method to estimate daily global averages of thermospheric mass density profiles using publicly available TLEs. In section 3 we benchmark our recovered atmospheric state from 2014 through 2026 against available reference data. Next, in section 4 we develop a second-pass augmentation for the solver to provide 6 hr temporal resolution for more recent (2022+) epochs. Finally, in section 5 we leverage the recent *Gershman* [2026a,b] parameterization of mass density at a fixed altitude from energy input indices to extrapolate the TLE-based profiles to NRT latencies.

2. Deriving Global-Averaged Mass Density

2.1 Calculating Drag Acceleration

In the absence of significant atmospheric motion, the drag acceleration term of an object in LEO can be approximated as,

$$\dot{\boldsymbol{v}}_{\boldsymbol{D}} \approx -\frac{1}{2}\rho B v^2 \boldsymbol{e}_{\boldsymbol{v}} \qquad (1),$$

where $\dot{\boldsymbol{v}}_{\boldsymbol{D}}$ is the drag acceleration vector, and $\boldsymbol{e}_{\boldsymbol{v}}$ is the object's unit velocity vector, v is the object's orbital speed, ρ is the mass density of the atmosphere, and B is the inverse ballistic coefficient defined as,

$$B = \frac{C_D A}{m} \qquad (2),$$

where C_D is the drag coefficient, A is the effective area of the object, and m is the object mass.

Following the initial derivation by *Picone et al.* [2005], we can generate daily-averaged drag accelerations from object tracking data as,

$$\langle \dot{v_D} \rangle \approx -\frac{\frac{1}{3}\mu^{2/3}\langle n_M \rangle^{-1/3}\Delta n_M \langle v \rangle^2}{\int v^3\left(1-\frac{r\omega}{v}\cos i\right)^2 dt} \quad (3),$$

Here, v is the speed of the object, μ is the gravitational parameter (3.986004418x10^{14} m^3/s^2 for Earth), and <> denotes a daily average. For simplicity we will not explicitly include <> notation going forward, but note that all time-varying quantities here correspond to daily-averaged parameters. In our implementation, $\dot{v_D}$ are calculated from publicly available Two-Line-Element (TLE) data. The derivation of these drag accelerations does not require any assumption about object ballistics or atmospheric properties.

2.2 Identification of Ballistically Stable Objects

From *Gershman* [2026a,b], variations in $\dot{v_D}$ for an near-circular object experiencing orbital decay are well-represented by a linear combination of the variations in the solar (S) and geomagnetic (G) energy inputs into the upper atmosphere, i.e.,

$$|\dot{v_D}| \approx \exp\left(\frac{-(z-z_o)}{H}\right)(\alpha S(t) + \beta G(t - T_o) + \gamma) \qquad (4)$$

where z is the object's altitude, z_o is a reference altitude at the start of the fit window, and α, β, γ, T_o, and H are constant parameters over the fit window. The exponential term allows for a scale-height (H) varying atmosphere to accommodate low altitude satellites experiencing re-entry. T_o encodes a time delay between the energy input and the atmospheric response.

Equation (4) will not provide a suitable approximation for $\dot{v_D}$ during active maneuvers such as altitude station-keeping or significant variations in attitude that impact a satellite's A/m ratio. For example, Starlink satellites, which undergo tremendous numbers of station-keeping maneuvers [*Berger et al.,* 2023; *Fitzpatrick et al.,* 2025] that are too frequent capture in daily-averaged TLEs are not well modeled by this parameterization. We use low-pass-filtered F10.7 (48h time constant) and AE (9h time constant) indices for S and G, respectively, as these data are available with manageable latency and over long observational baselines. The AE index, being sensitive to low level magnetic fluctuations in the auroral zone is particularly well-suited to fit subtle variations in $\dot{v_D}$ during on short time scales during both solar minimum and solar maximum conditions [*Rostoker*, 1972]. A 'root mean square percentage error' (RMSPE) metric of <0.15 was adopted as our quality fit criterion. We apply a 27-day (i.e., one solar rotation) fit window to all tracked objects with near-circular orbits (i.e., eccentricities <0.01), mean altitude less than 500 km, and altitude changes less than 2 km/day. As shown in Figure 1, there are 1000+ objects each day that meet this goodness of fit criteria in recent epochs. This approach results in the automated generation of a database of ballistically stable objects that can be used to aid atmospheric inversion efforts.

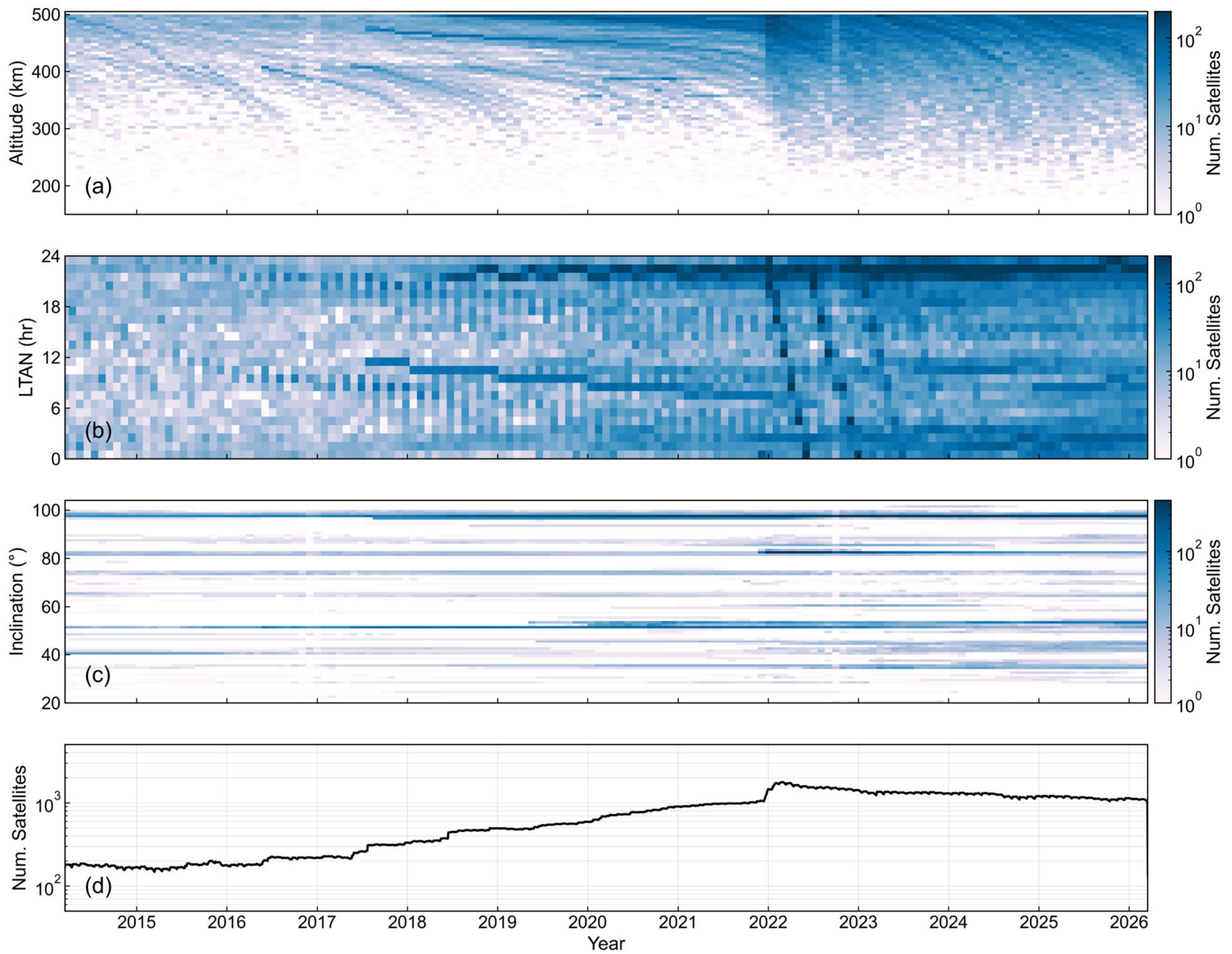

Figure 1. Overview of ballistically stable LEO objects from January 2014 to March 2026 used to solve for variations in the upper atmosphere organized by (a) altitude, (b) LTAN, (c) inclination, and (d) the total number as a function of time. At present there are 1000+ objects each day across a wide variety of orbits whose measured drag accelerations are highly correlated with energy inputs.

2.3 Solving for the Relative Atmosphere

In order to constrain atmospheric variation with altitude (z), we adopt the J70 model [*Jacchia*, 1970], where a single temperature T_{eff} (nominally the value at the top of the atmosphere) parameterizes the shape of ρ(z). Other models (e.g., MSIS) would also be suitable here, with the only requirement that their average altitude profile shape be parameterizable. Because we are not aiming to resolve the density profiles of individual species, T_{eff} is not necessarily a physical temperature but rather an altitude 'shape' parameter. We also define a 'scale' parameter, C, such that,

$$\rho(z) \approx C\ \rho_{J70}(z, T_{\mathrm{eff}}) /\ \rho_{J70}(z_{\mathrm{ref}}, T_{\mathrm{eff}}). \qquad (5)$$

C is therefore the effective mass density at reference altitude z_{ref}, taken here as 400km.

We combine equation (1) and (5) and take the logarithm of both sides to form a set of equations for a given satellite i,

$$\log\left|\frac{2\dot{v_{D_i}}}{v_i^2}\right| - \log\langle B_i\rangle - \log C - \log \rho_{J70}\,(z_i, T_{\mathrm{eff}}) + \log \rho_{J70}\,(z_{\mathrm{ref}}, T_{\mathrm{eff}}) \approx 0 \qquad (6)$$

where $\dot{v_{D_i}}$, v_i , and z_i are the daily averaged quantities per satellite i, $\langle B_i\rangle$ corresponds to the average inverse ballistic coefficient over all observations per satellite, and C and T_{eff} are daily-varying parameters that describe the atmospheric profile. Equations of the form (6) are then put into a non-linear least squares solver to determine per satellite $\langle B_i\rangle$ and per day C and T_{eff}. As shown in Figure 2, this fit results in a relative global atmospheric density profile as a function of time. A single overall constant (here, 1.6063) is then applied to scale this relative solution to absolute units, which was chosen to minimize systematic errors between the model and available reference data.

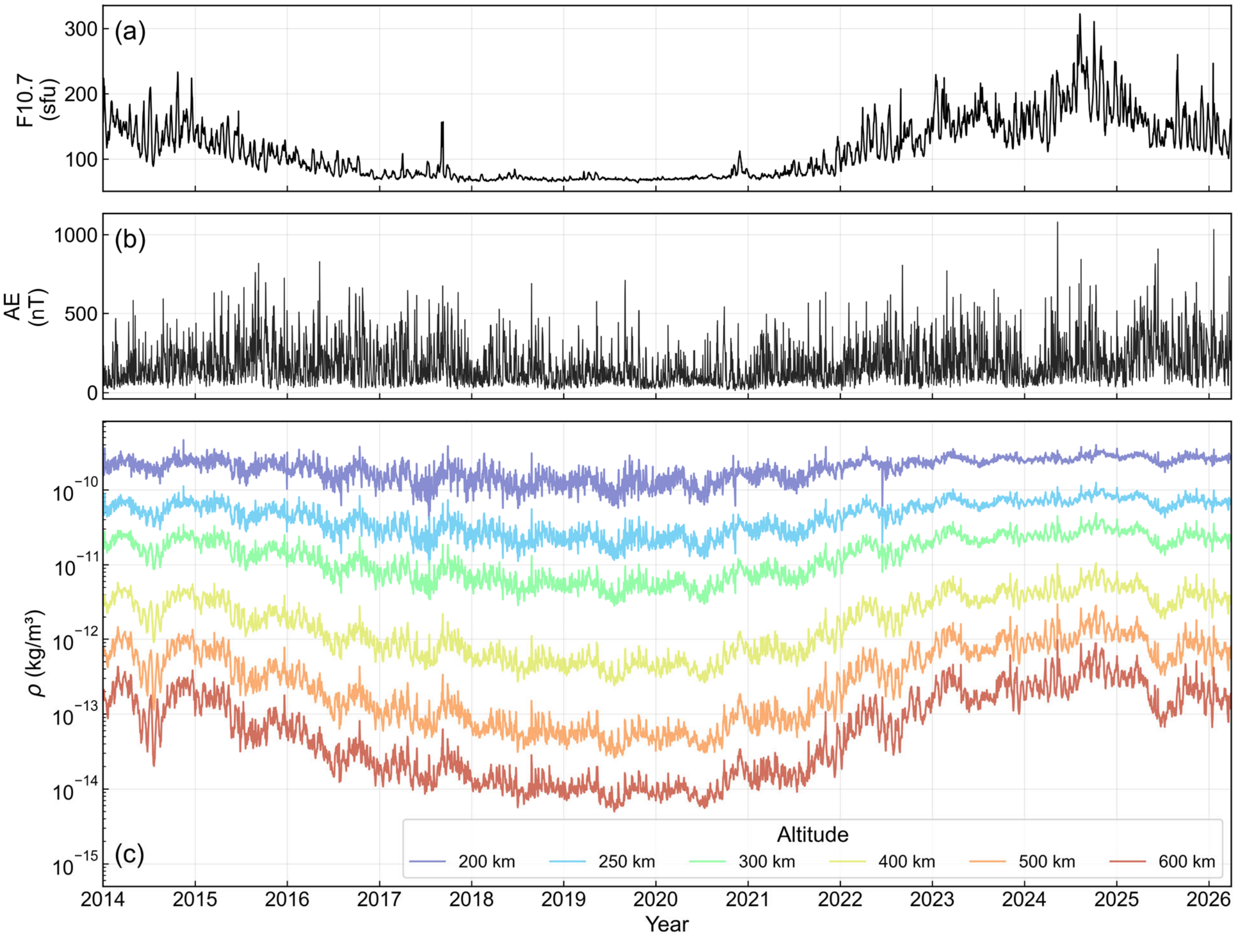

Figure 2. (a) Solar (F10.7) and (b) geomagnetic (AE index) energy sources used to parameterize drag acceleration for LEO objects and aid in the filtering of ballistically stable objects suitable for use in the atmospheric inversion solver. (c) Global-average daily atmospheric density from 200km to 600km calculated using publicly available TLEs. Satellites from all LTAN and inclinations bins are from Figure 1 are included in the global average.

3. Daily-Averaged Model Validation

Now we compare our daily-averaged $\rho(z)$ profiles with available reference data, namely: (1) the TLE2021 model, (2) spacecraft-derived in situ mass densities from GRACE, and (3) a selected set of HASDM intervals. As discussed by *Bruinsma et al.* [2023], there are systematic uncertainties associated with all datasets, some of which are not fully quantified or understood, though all being in agreement to ~20% of one another. We will demonstrate that our model results are 'in-family' with these references.

3.1 TLE2021

The TLE2021 [*Emmert et al.* 2021b] is a TLE-derived dataset of global-average density at 10 fixed altitudes from 200km to 575km between 1967 and 2019. The model is intended to provide a long-term reference for thermospheric variability. First, model dependent (NRLMSISE-00) ballistic coefficients are calculated for each object, and calibrated against a set of ~200 reference objects. The corresponding density ratios are then used to fit global NRLMSISE-00 averages. As shown in Figure 3, we can compare our daily averages from 2014 to 2019 with those from TLE2021. We find mean (μ) and standard deviation (σ) ratios between the models at altitudes 250km, 400km, and 575 km of -3.8±14.7%, -0.2±8.0%, and -2.0±12.6%, respectively, indicating good agreement, with higher variability expected here due to the effective averaging over ~3 days for most data points in TLE2021.

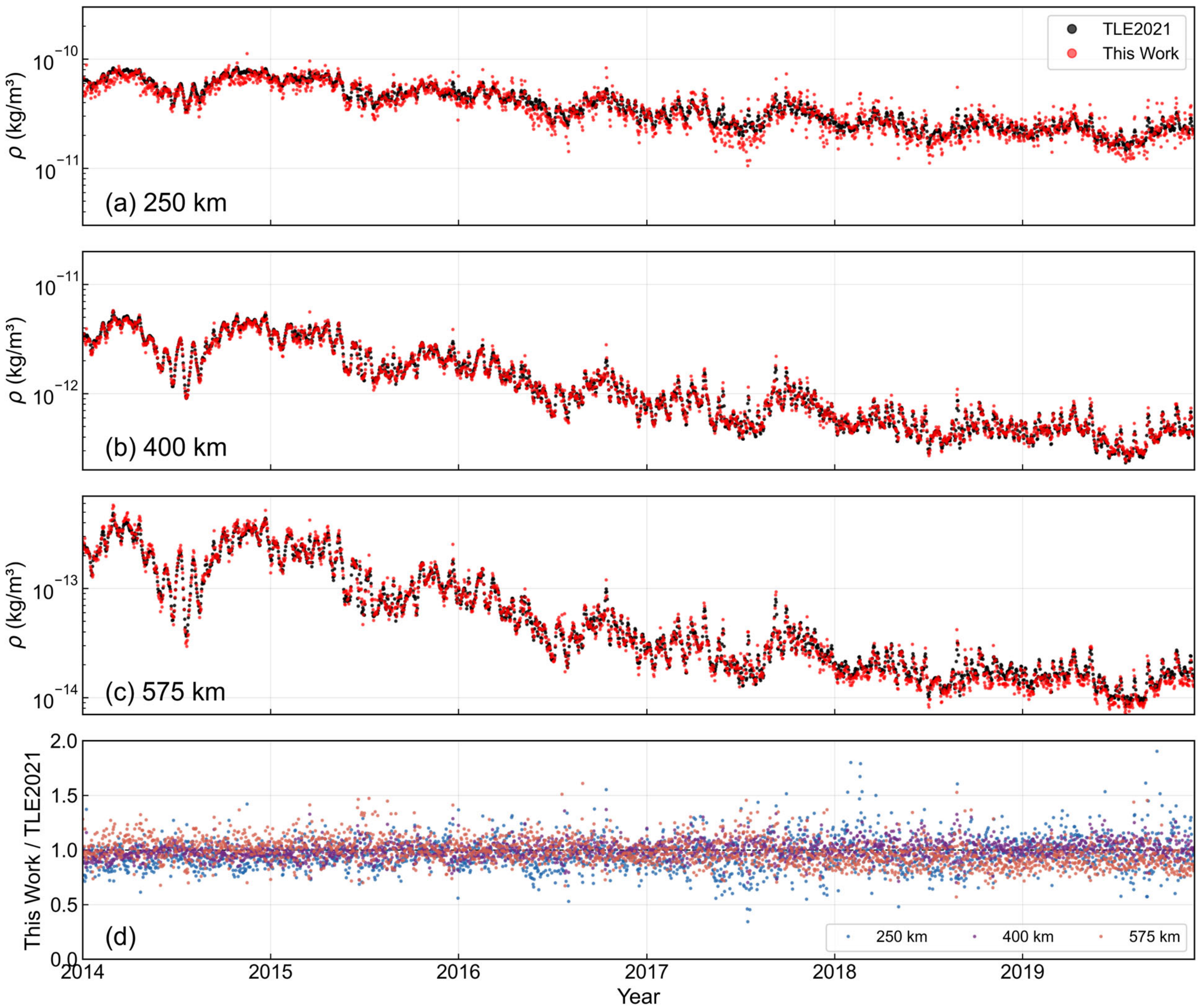

Figure 3. Mass density at (a) 250 km, (b) 400km, and (c) 575km calculated from 2014 through 2019 from TLE data using the technique described here (red dots) and from the TLE2021 model (black dots) from *Emmert et al.* [2021b]. The ratio between the the two model is shown in (d). Overall there is good agreement between the two estimates of thermospheric mass density.

3.2 GRACE

The GRACE satellites use precise accelerometers and carefully-modeled spacecraft drag coefficients to derive neutral mass density at ~10s cadence along-track. While there are significant variations associated with spatial structure along orbit, daily-averaged data provides a solid absolute density reference. In Figure 4 we show a comparison between our model and daily-average GRACE data. We find ratios of 6.6±21.8% and 1.1±25.0% for the GRACE A and GRACE-FO satellites, respectively. The larger variability observed here (our model vs GRACE) compared to Section 3.1 (our model vs. TLE2021) model is attributed to comparing a single-spacecraft along-track density for GRACE with a global average.

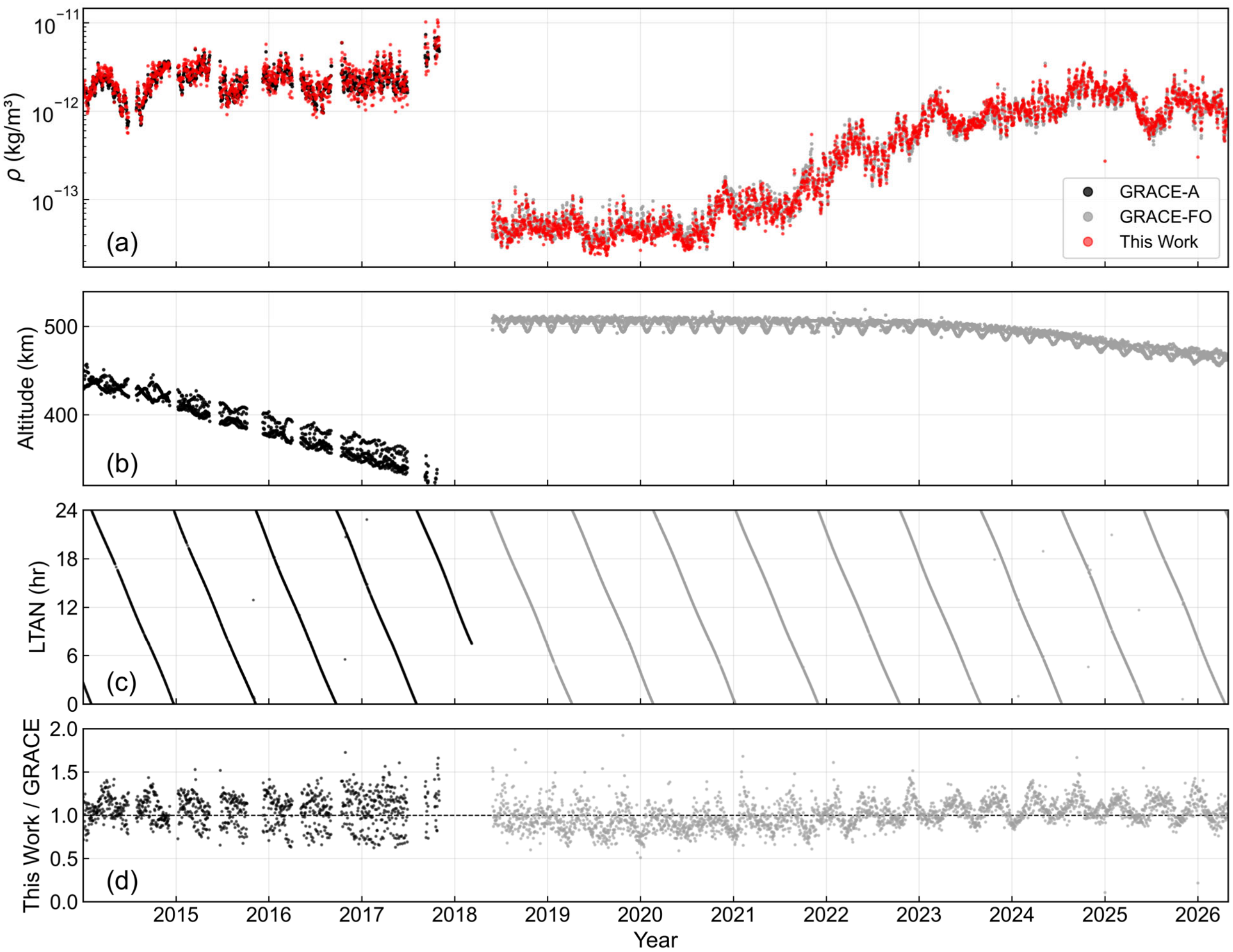

Figure 4. (a) Mass density calculated here (red dots) and those measured by GRACE A (black dots) and GRACE-FO (gray dots) from 2014 to present. (b) Altitude and (c) LTAN of each satellite are shown, as well as (d) the ratio between our model and the reference data. Because GRACE satellites sample along an orbit rather than a global average, there are periodicities in the comparison, though the baseline level is in agreement.

3.3 HASDM

HASDM provides 3 h mass density from 175 to 825km in 25 km bins over a 10º in latitude and 15º in local time solar grid [*Storz et al.* 2005]. Although its operational data products are not public, historical data is available for reference. Here, as shown in Figure 5, we perform daily and global averaging of the HASDM data for three 6 month intervals, each of which representing a different phase of the solar cycle (declining phase, solar minimum, solar maximum). At altitudes of 250km, 400km, and 575km we find differences of ≲15%, summarized in Table 1. The largest discrepancy occurs at low altitudes, consistent with that reported by *Bruinsma et al.* [2023] for a systematic TLE2021-HASDM comparison.

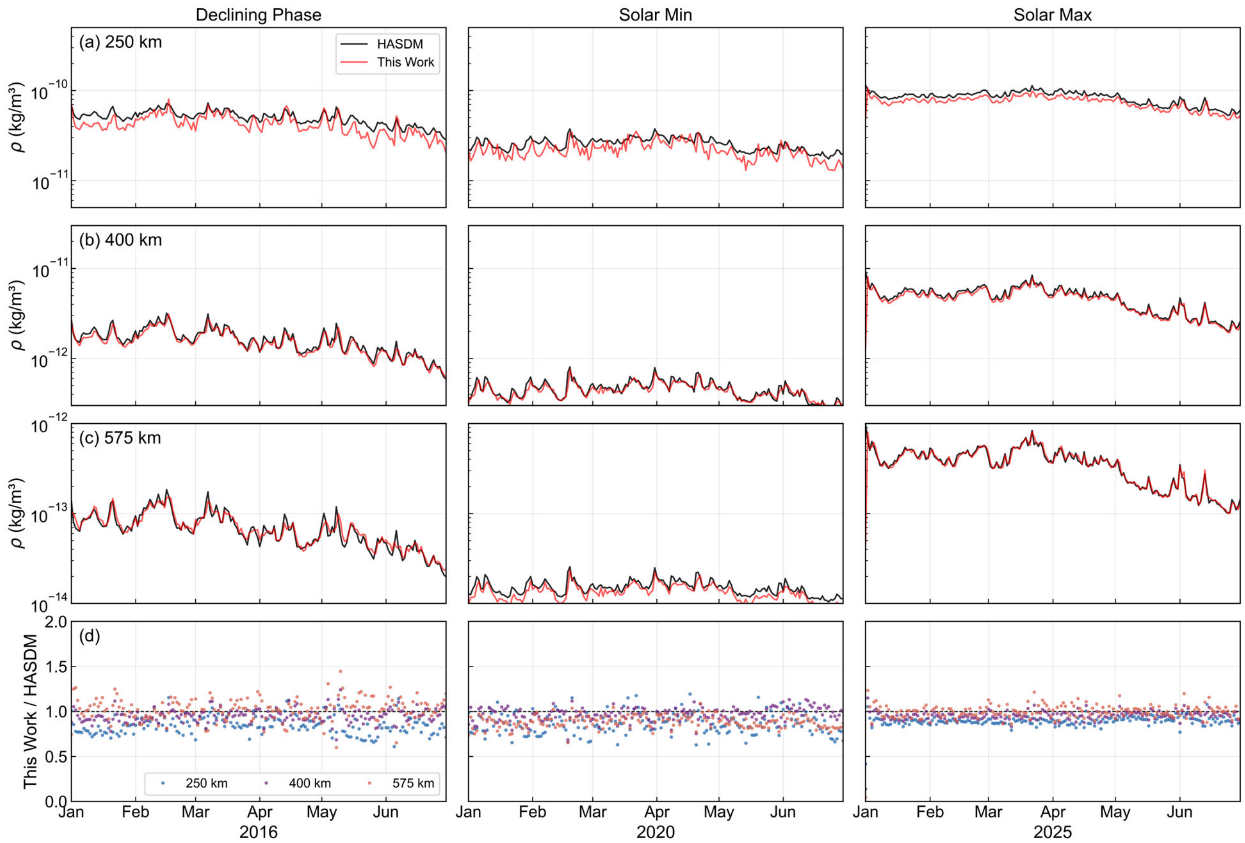

Figure 5. Six month intervals set during (left) the declining phase of the solar cycle, (middle) solar minimum, and (right) solar maximum. Mass density profiles from our model (red curve) and HASDM (black curve) are shown for (a) 250km, (b) 400km, and (c) 575km, with the ratio between them shown in panel (d). There is overall agreement between the two models, in particular with the day-day variability, with the largest systematic discrepancy of (~10-15%) observed at low altitudes.

Table 1. Comparison of our model with globally averaged mass densities from HASDM for the three example intervals shown in Figure 5.

Altitude (km)	Declining	Solar Min	Solar Max
250	-15.4±9.7%	-13.6±11.2%	10.7±3.8%
400	-4.7±8.4%	-2.4±10.0%	-4.5±6.7%
575	2.8±14.6%	-11.2±9.4%	0.4±11.5%

4. Achieving Sub-Daily Time Resolution

The data derived in Section 2 uses daily averaging, which was found to be necessary to achieve quality measured $\dot{v}_D$ values from TLE data. However, many LEO objects have multiple TLEs released per day, each of which encodes valuable information about the sub-daily variations in drag acceleration in the form of its reported B^* values. B^* is a fit parameter in the SGP4 orbit propagator that combines the satellite's effective drag *A/m* ratio with a fixed reference density, absorbing both the ballistic coefficient and any mismatch between the true atmospheric density and SGP4's internal density model. This coupling complicates its direct use in the atmospheric inversion described in Section 2. However, on short time scales, in particular for ballistically stable satellites with minimal changes in altitude, variations in B^* should be proportional to variations in ρ. Anchored by the daily-averaged mass density profiles validated in Section 3, we can leverage sub-daily B^* data to recover finer time resolution variations in the upper atmosphere.

We identify a focused subset of satellites from Figure 1, i.e., those with mean altitudes between 400-450km and decay less than 0.5 km/day in a given 27 day window. These objects are not only ballistically stable but also require minimal relative altitude scaling to our reference altitude z_{ref}. As an example, in Figure 6 we show B^* values from 86 such satellites in May 2024. The sets of B^* values exhibit similar variations but with different overall scaling per satellite. We use daily-averaged T_{eff} to scale measured B^* data to z_{ref} and then scale each day's altitude-adjusted B^* values to match the daily-averaged density C (from eq. 5). After taking the median across all satellites for within a specified time cadence (e.g., 6h), we recover a sub-daily C time series.

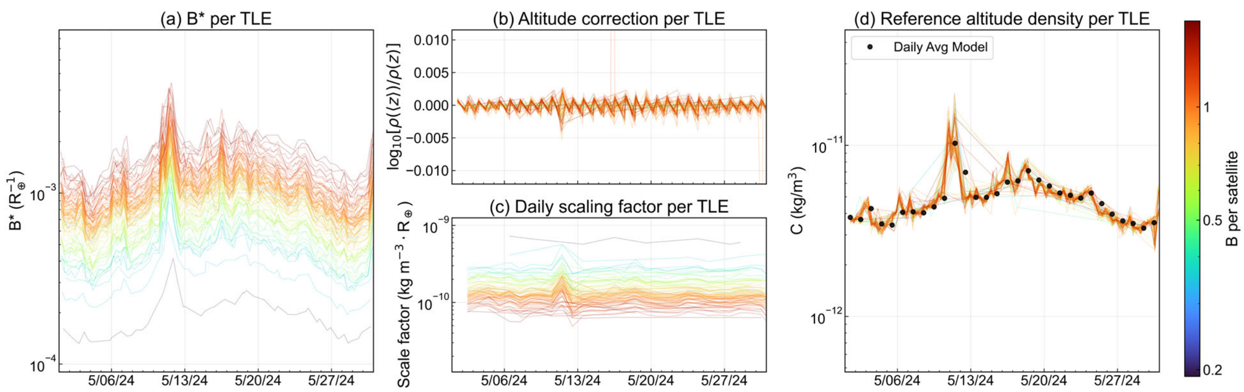

Figure 6. (a) Raw B^* values for the month of May 2024 for 86 satellites used in the high altitude pool. Variations track each other but at different levels ordered by their inverse ballistic coefficient (colors derived via daily average model). Raw values are then corrected for (b) altitude and (c) daily scalings derived from the daily-average fit to recover a high time resolution time series in (d) at a reference altitude.

To recover the sub-daily altitude profile of the atmosphere, we make use of the fact that on short time scales, the shape and scale of the atmosphere at z_{ref} are linearly related (i.e., ΔC is proportional to ΔT_{eff}). As demonstrated in Figure 7, which shows daily-averaged C and T_{eff} for May 2024, this approximation holds even during the extreme Gannon Storm, where Dst reached -412 nT [*Hayakawa et al.,* 2025]. By enforcing this best-fit linear relationship, we can use sub-daily C to calculate corresponding T_{eff} parameters, resulting in fine time resolution altitude profiles of mass density.

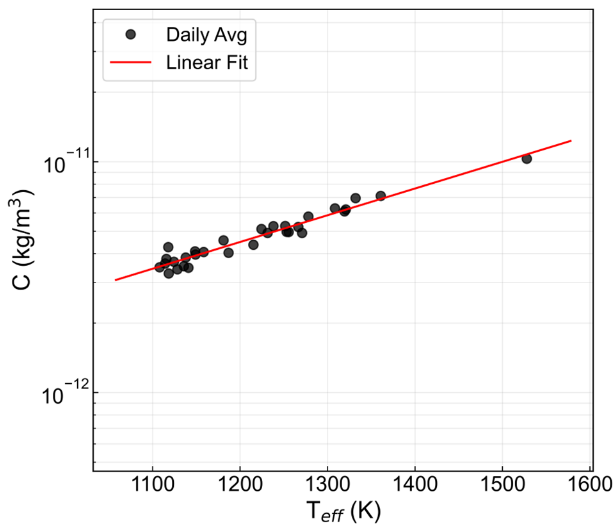

Figure 7. C vs T_{eff} parameters as derived from the daily-average solver for May 2024. Data are well correlated and well-represented on this short time scale by a linear relationship (red line) that can be used to connect within-day variations in altitude profile shape with variations in altitude profile scale, and vice versa.

We can validate our recovered 6h data product with global-averaged HASDM data, analogous to the comparison in Figure 5 at higher cadence. As shown in Figure 8, we find percent differences of (-14.6±3.6%, -10.5±4.3%, -7.9±5.1%, -4.0±7.0%, -0.7±9.3%, 1.6±11.8%) at altitude bins of (200km, 250km, 300km, 400km, 500km, and 600km), respectively, on par with the corresponding daily-averaged metrics.

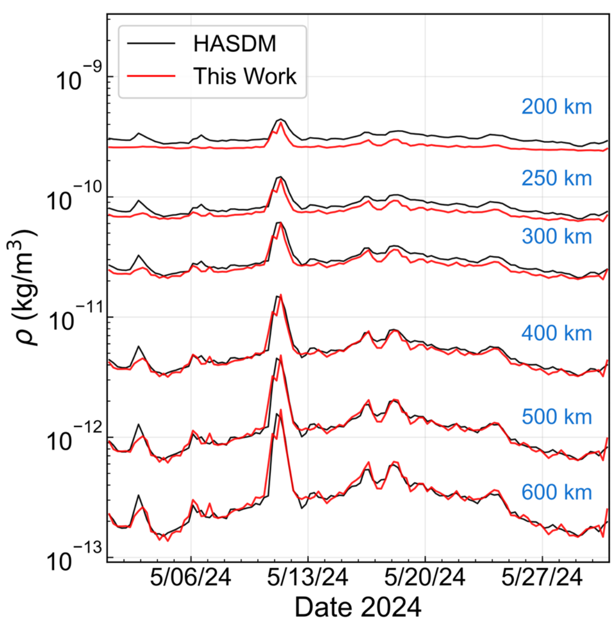

Figure 8. Daily-averaged model augmented with sub-daily TLE B* variations averaged to 6 hours (red curves) and corresponding HASDM (black curves) data for May 2024. As with the daily averaged comparison in Figure 5, there is solid agreement between the two models even during the extreme Gannon Storm on May 11, with the largest systematic discrepancy (~15%) at low altitudes.

Application of this technique requires a sufficient number of satellites to be both ballistically stable and in the right range of altitudes. We find that sub-daily variations become regularly possible to recover for epochs after 2022, enabling their use for current operations.

5. Density Extrapolation to Near Real Time

The TLE-derived density model discussed in Sections 2 through 4 will provide the state of the atmosphere with ~24 h latency. To extrapolate these densities to the current epoch, we again utilize the *Gershman* [2026a,b] approach, used here not to filter objects but rather to parametrize variations in ρ in terms of solar and geomagnetic energy sources. We model the daily-averaged density ρ at z_{ref} using,

$$\rho \approx \rho_s + \rho_G \approx (aS + c) + b\,G \quad (7)$$

where *a*, *b*, and *c* are the set of fit parameters at a fixed altitude and ρ_s and ρ_G are the densities associated with solar and geomagnetic input, respectively. We fit on daily-averaged ρ for coefficient stability; finer-cadence evaluation is performed by substituting higher-cadence drivers post-fit. To ensure anchoring to the most recent data, we use a 7d fit window ending with the last available daily average.

Unlike the filter in Section 2.2 (which uses longer-baseline F10.7 and AE indices), NRT extrapolation requires drivers with low operational latency, so we substitute GOES EUVS [*Eparvier et al.,* 2009] for solar and ap [*Matzka et al.* 2021] for geomagnetic input. We sum GOES-R EUVS irradiance across its 256Å, 284Å, and 304Å channels, daily-average, and apply a 48h low pass filter (LPF). We take ap, available approximately 30 minutes after each 3h observation window, assume persistence to the current epoch, daily-average, and apply a 9h LPF. The 9-h smoothing window is wide compared to the latency between the most recent ap measurement and the current epoch (<3.5 h), so persistence-assumed values introduce minimal error in *G*.

Once the fit parameters *a*, *b*, and *c* are recovered, we apply them to the highest available cadence *S* and *G* data, resulting in a fine time resolution estimate of ρ at z_{ref}. Finally, we leverage the linear relationship between *C* and T_{eff} calculated over the fit window to recover full altitude profiles of ρ up to the current epoch. Examples of the fit and extrapolation are shown in Figure 9 for quiet (Nov-Dec 2022) and active (Apr-May 2024) periods. As expected, the data are well parameterized by a linear combination of energy inputs over the 7d fit window, and minimal distortions are observed when extrapolating up to 36 h.

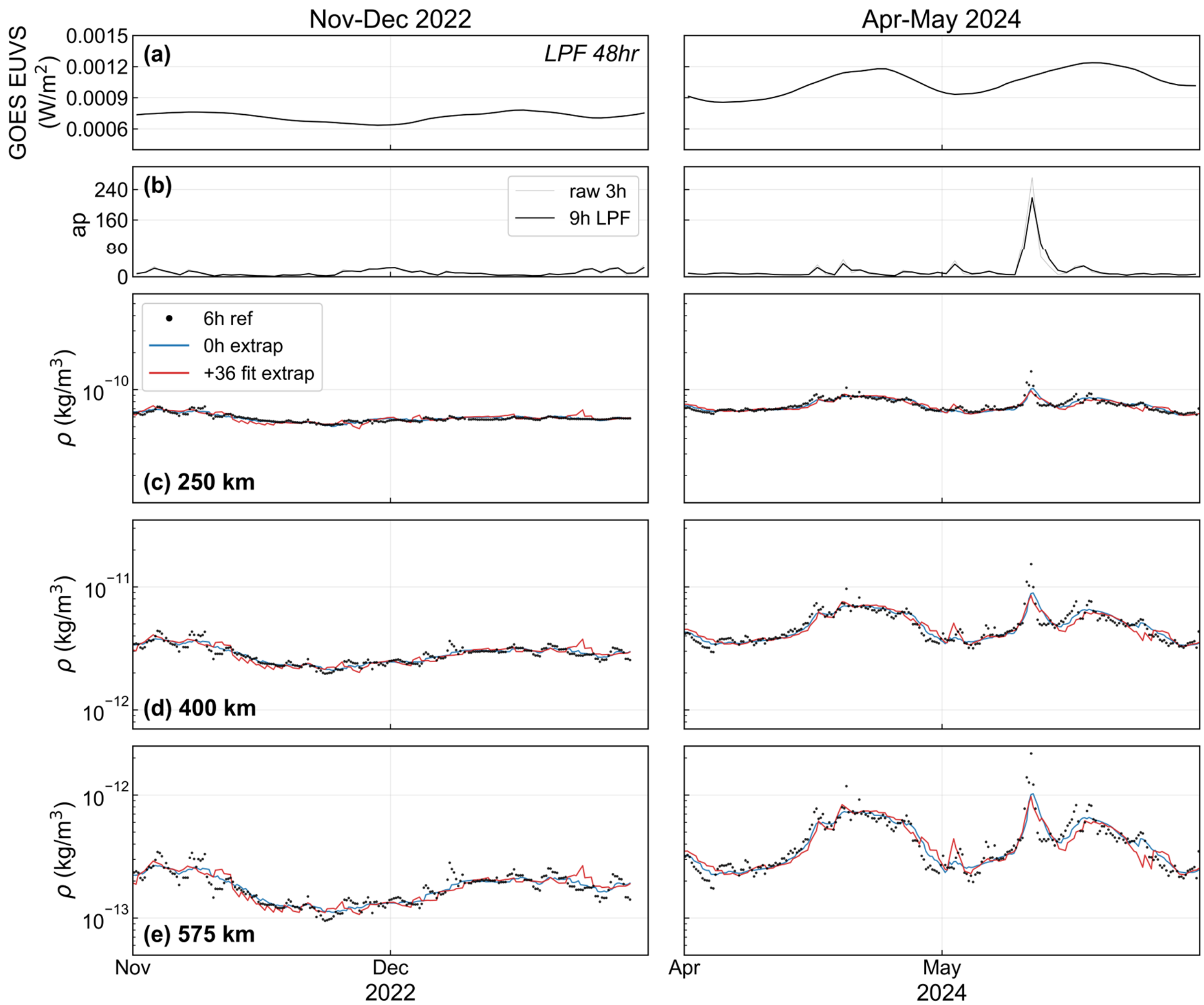

Figure 9. (a) Solar driver S (GOES EUVS), (b) geomagnetic driver G (ap index), and mass density at (c) 250 km, (d) 400 km, and (e) 575 km during a quiet interval (Nov-Dec 2022, left) and an active interval (Apr-May 2024 Gannon storm, right). Reference 6 h densities from the TLE-anchored solver are shown as black dots; the fit is overlaid for (blue) 0 h and (red) +36 h extrapolation horizons. Both horizons track the reference data closely, with the largest discrepancies during peak geomagnetic activity.

We can systematically evaluate the effectiveness of our approach by calculating the relative error of the fit compared to our 6 h TLE-derived density reference as a function of geomagnetic activity (i.e., max 3h ap value in a day defines G0 through G5 [*Poppe,* 2000]). In Figure 10 we show the μ and σ for different extrapolation times up to 72 h. The model exhibits very little systematic bias (i.e., |μ| < 5%) for extrapolations under 36h. σ increases both with geomagnetic activity and extrapolation time, rising above ~20% after ~36 h under storm conditions.

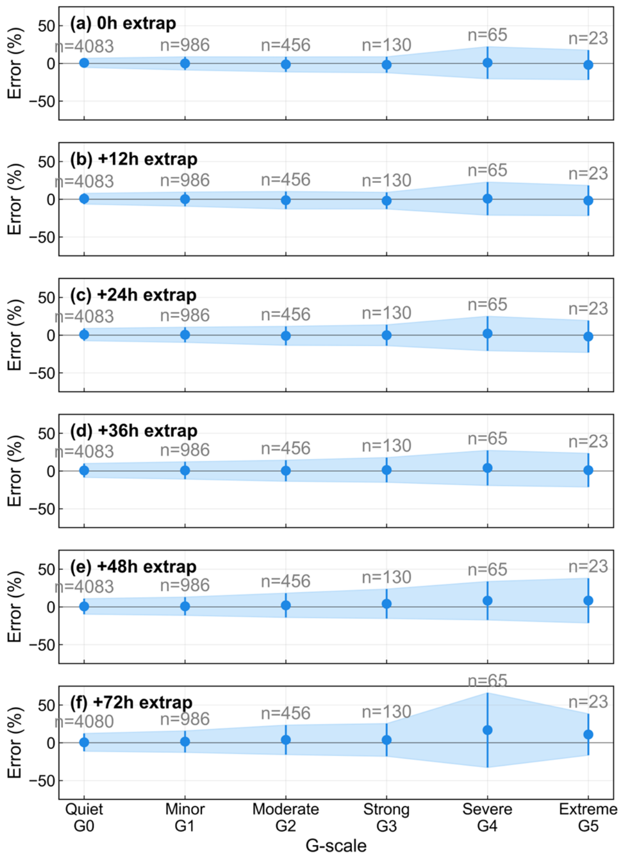

Figure 10. Systematic (μ) and variability (σ) errors of the parameterization of TLE-derived densities by solar and geomagnetic drivers, binned by G-class (max raw 3 h ap per day), at (a) 0 h, (b) +12 h, (c) +24 h, (d) +36 h, (e) +48 h, and (f) +72 h extrapolation horizons. Errors grow with both geomagnetic activity and horizon time, in particular beyond ~36 h.

Finally, we summarize our overall NRT monitoring pipeline in Figure 11. Our approach consists of three main elements: (1) a TLE-based solver for delayed-epoch (~24 h) daily-averaged atmospheric density profiles, (2) an optional B*-anchored augmentation for 6 h resolution when satellite coverage permits, and (3) a density extrapolator that uses energy source indices to bridge the gap to NRT latencies.

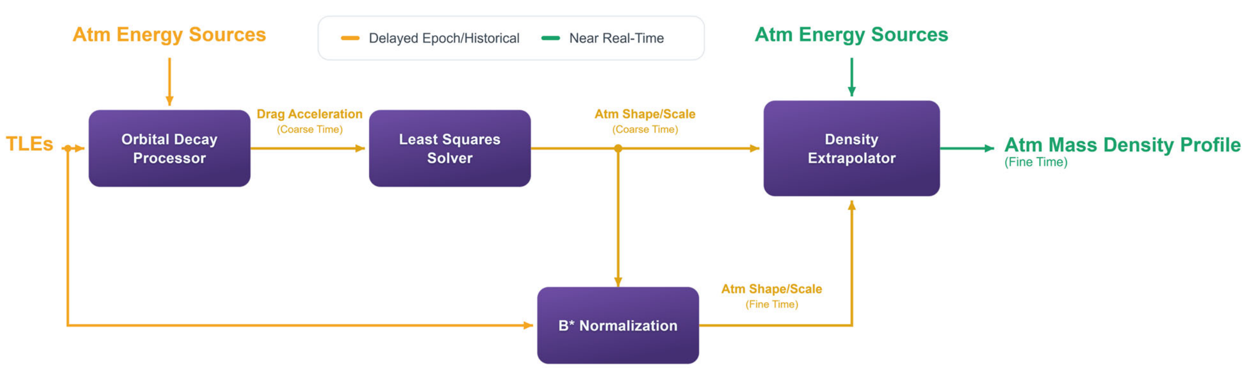

Figure 11. Generalized flow diagram of developing delayed-epoch, fine-cadence atmospheric density estimates from TLE data, and extrapolating profiles to NRT latencies.

6. Discussion

The elements developed here provide complementary yet independent methods to (1) achieve recent atmospheric mass density profiles from TLEs and (2) extrapolate a reference density profile using solar and geomagnetic indices. Together these components enable NRT monitoring of the upper atmosphere using public data. However, one could also either apply extrapolation to an alternatively sourced density reference profile or link the TLE densities to a different model driven by solar and geomagnetic energy sources. For example, our TLE-derived densities provide the equivalent of pre-storm baseline correction required by more comprehensive empirical atmospheric models to achieve improved performance [*Kalafatoglu Eyiguler et al.,* 2019; *Bruinsma et al.,* 2021; *Bruinsma and Laurens,* 2024; *Wang et al.,* 2026]. Our global-average values could also be used to scale or constrain a more detailed thermospheric model that includes spatial structure and/or improved physics at high (i.e., >600 km) or low (i.e., <200 km) altitudes.

The choices of fit window size, *S* and *G* sources, and data pre-conditioning (e.g., LPF bandwidth) will all impact fit accuracy and valid extrapolation horizon. Here we intended to illustrate the potential for these techniques in enabling NRT monitoring, but did not exhaustively optimize model inputs. For example, composite indices or more complex pre-conditioning may be needed to more accurately resolve the details of storm risetime and recovery (e.g., *Bowman et al.,* [2008]). In addition, other driver data may yet become available that provide more robust parameterization of the relevant energy sources, lower latencies, or both.

Finally, although this study has focused on nowcasting, the presented framework also extends to forecasting. Because atmospheric response lags energy input, the latest available *S* and *G* data actually support forecasts several hours into the future. In addition, with known fit parameters, forecasted *S* and *G* drivers rather than measured quantities can be used to generate corresponding atmospheric mass density profile estimates. Given the challenges in predicting geomagnetic drivers, one additional advantage of our decomposition of the density into ρ_S and ρ_G components is the ability to constrain changes in the upper atmosphere based on activity level. As demonstrated by *Gershman* [2026b], with a known ρ_S baseline and established relationship between *G* and ρ_G, one can generate different atmospheric profile scenarios (e.g., geomagnetically quiet, intense, extreme) using corresponding ranges of *G*. Such scenarios can be used to generate physically-informed uncertainties in re-entry predictions or for constraining the altitude loss experienced by a given object during a geomagnetic storm.

7. Concluding Remarks

We have demonstrated that public TLE data combined with standard space-weather indices can produce thermospheric density profiles in agreement with established references (TLE2021, GRACE, HASDM) across 200-600 km. In addition, our density extrapolator maintains accuracy over +36 h time horizons, supporting both nowcast and short-term forecast applications even during extreme geomagnetic activity. Because our TLE-based solver and index-driven extrapolator are independent modular elements, either component can be swapped for proprietary, higher-fidelity, or future alternatives as they become available. By relying only on public data and standard scientific software, this framework lowers the barrier for the LEO community to access the current state of the atmosphere.

Acknowledgements. This work was supported by the NASA Internal Research and Development Program. We gratefully acknowledge A. Glocer for his feedback on this manuscript. We acknowledge the use of Claude (Anthropic, claude.ai) for manuscript editing, code execution, and data processing. The AI tool largely implemented and executed the code logic. We subsequently vetted all generated outputs and checked critical algorithmic components to ensure the correct mathematical and conceptual implementation of the presented model. We take full responsibility for the data integrity and final results.

Data used in this study were obtained from the following sources:

- **TLE data** - Space-Track gp_history class (2005–2026, raw two-line elements per NORAD ID): https://www.space-track.org/basicspacedata/query/class/gp_history/
- **TLE2021** - NRL orbit-derived global-mean density v2.0 (1967–2019). Files used: orbit-density-ds03-density-values.txt (absolute $\log_{10}\rho + \sigma$, 10 alts 250–575 km, daily), orbit-density-ds01-objects-used.txt (BC reference set): https://map.nrl.navy.mil/map/pub/nrl/orbit_derived_density/v2.0_1967-2019/
- **HASDM** - SET/USSF JB2008-HASDM gridded density (10 alts 175–825 km, 3-hourly, 15°×20° lat/lon). Monthly ZIP files YYYYMM_HASDM.txt.zip obtained via SpaceWx portal: https://spacewx.com/hasdm/
- **GRACE A** - TU Delft V2 accelerometer densities GA_DNS_ACC_YYYY_MM_v02.zip (2002–2017): https://thermosphere.tudelft.nl/data/data/version_02/GRACE_data/
- **GRACE-FO** - TU Delft V2 GC_DNS_ACC_YYYY_MM_v02c.zip (2018–2026): https://thermosphere.tudelft.nl/data/data/version_02/GRACE-FO_data/
- **F10.7 index** - LISIRD/LASP mirror of NRCan/DRAO Penticton adjusted daily flux (1947–present): https://lasp.colorado.edu/lisird/latis/dap/penticton_radio_flux.csv
- **GOES-R EUVS** - L2 AVG1D 26–34 nm from GOES-16/17/18/19 (dn_euvs-l2-avg1d_g{16,17,18,19}_s{...}_e{...}_v1-0-7.nc): https://data.ngdc.noaa.gov/platforms/solar-space-observing-satellites/goes/goes{16,17,18,19}/l2/data/euvs-l2-avg1d/
- **AE index** - Kyoto WDC real-time digital ae{YYMMDD} (1-min AE/AL/AO/AU): https://wdc.kugi.kyoto-u.ac.jp/ae_realtime/
- **ap / Kp indices** - GFZ Potsdam Kp_ap_Ap_SN_F107_since_1932.txt (Kp/ap 3-hourly, Ap daily, since 1932): https://kp.gfz-potsdam.de/app/files/Kp_ap_Ap_SN_F107_since_1932.txt

References

Akmaev, R. A. (2011), Whole atmosphere modeling: Connecting terrestrial and space weather, Rev. Geophys., 49, RG4004, doi:10.1029/2011RG000364.

Berger, T. E., Dominique, M., Lucas, G., Pilinski, M., Ray, V., Sewell, R., et al. (2023). The thermosphere is a drag: The 2022 Starlink incident and the threat of geomagnetic storms to low earth orbit space operations. *Space Weather*, 21, e2022SW003330. https://doi.org/10.1029/2022SW003330

Bowman, B., Tobiska, W. K., Marcos, F., Huang, C., Lin, C., & Burke, W. (2008). A new empirical thermospheric density model JB2008 using new solar and geomagnetic indices. In *AIAA/AAS Astrodynamics Specialist Conference and Exhibit*, Honolulu, Hawaii. https://doi.org/10.2514/6.2008-6438

Bruinsma, S., & Boniface, C. (2021). The operational and research DTM-2020 thermosphere models. *Journal of Space Weather and Space Climate*, EDP sciences, **11**, 47-1–47-15. https://doi.org/10.1051/swsc/2021032

Bruinsma, S., & Laurens, S. (2024). Thermosphere model assessment for geomagnetic storms from 2001-2023. *Journal of Space Weather and Space Climate*, **14**, 28. https://doi.org/10.1051/swsc/2024027

Bruinsma, S., Dudok de Wit, T., Fuller-Rowell, T., Garcia-Sage, K., Mehta, P., Schiemenz, F., et al. (2023a). Thermosphere and satellite drag. *Advances in Space Research*. https://doi.org/10.1016/j.asr.2023.05.011

Bruinsma, S., Siemes, C., Emmert, J. T., & Mlynczak, M. G. (2023b). Description and comparison of 21st century thermosphere data. *Advances in Space Research*, **72**(12), 5476–5489. https://doi.org/10.1016/j.asr.2022.09.038

Bruinsma, S., Boniface, C., Sutton, E. K., & Fedrizzi, M. (2021). Thermosphere modeling capabilities assessment: Geomagnetic storms. *Journal of Space Weather and Space Climate*, **11**, 12. https://doi.org/10.1051/swsc/2021002

Burke, W. J. (2018). Thermospheric dynamics during the March 1989 magnetic storm. Balkan, Black sea and Caspian sea regional network for space weather studies. https://doi.org/10.31401/SunGeo.2018.02

Emmert, J. T. (2015), Altitude and solar activity dependence of 1967–2005 thermospheric density trends derived from orbital drag. *J. Geophys. Res. Space Physics*, 120, 2940–2950, doi: 10.1002/2015JA021047.

Emmert, J. T., Drob, D. P., Picone, J. M., Siskind, D. E., Jones, M. Jr., Mlynczak, M. G., et al. (2021a). NRLMSIS 2.0: A whole-atmosphere empirical model of temperature and neutral species densities. *Earth and Space Science*, 8, e2020EA001321. https://doi.org/10.1029/2020EA001321

Emmert, J. T., Dhadly, M. S., & Segerman, A. M. (2021b). A globally averaged thermospheric density data set derived from two-line orbital element sets and special perturbations state vectors. *Journal of Geophysical Research: Space Physics*, 126, e2021JA029455. https://doi.org/10.1029/2021JA029455

Eparvier, F.G., et al. "The Extreme Ultraviolet Sensor (EUVS) for GOES-R", Proc. SPIE 7438, Solar Physics and Space Weather Instrumentation III, 743804 (23 Sept 2009); https://doi.org/10.1117/12.826445

Fitzpatrick, D. J., Sutton, E.K., Pilinski, M. D., et al. (2025), Harnessing Satellite Constellations as Signals of Opportunity for an Enhanced Specification of the Satellite Drag Environment in the Critical LEO Regime. *Authorea.* https://doi.org/10.22541/au.176244733.31846582/v1

U.S. Government Accountability Office. (2022). Large Constellations of Satellites:Mitigating Environmental and Other Effects, *GAO-22-105166*. https://www.gao.gov/products/gao-22-105166

Gershman, D. J. (2026a), Quantifying the Impacts of Solar and Geomagnetic Activity on Objects in LEO, *NASA Technical Memorandum*, NASA/TM-20260001916, https://dx.doi.org/10.64631/BCHL4158

Gershman, D. J. (2026b), Parameterization of Satellite Drag Acceleration Without the Use of A Global Thermosphere Model, *NASA Technical Memorandum*, NASA/TM-20250011658, https://dx.doi.org/10.64631/LUGN8147

Hayakawa, H., Ebihara, Y., Mishev, A., Koldobskiy, S., Kusano, K., Bechet, S., Yashiro, S., Iwai, K., Shinbori, A., Mursula, K., Miyake, F., Shiota, D., Silveira, M. V. D., Stuart, R., Oliveira, D. M., Akiyama, S., Ohnishi, K., Ledvina, V., & Miyoshi, Y. (2025). The Solar and Geomagnetic Storms in May 2024: A Flash Data Report. The Astrophysical Journal, 979 (1). https://doi.org/10.3847/1538-4357/ad9335

Jacchia, L. G. (1970). New static models of the thermosphere and exosphere with empirical temperature profiles, *Spec. Rep* (Vol. **313**). Cambridge, Massachusetts: Smithson, Astrophys. Obs.

Kalafatoglu Eyiguler, E. C., Shim, J. S., Kuznetsova, M. M., Kaymaz, Z., Bowman, B. R., Codrescu, M. V., et al. (2019). Quantifying the storm time thermospheric neutral density variations using model and observations. *Space Weather*, 17, 269–284. https://doi.org/10.1029/2018SW002033

Licata, R. J., Mehta, P. M., Weimer, D. R., Tobiska, W. K., & Yoshii, J. (2022). MSIS-UQ: Calibrated and enhanced NRLMSIS 2.0 model with uncertainty quantification. *Space Weather*, 20, e2022SW003267. https://doi.org/10.1029/2022SW003267

Matzka, J., Stolle, C., Yamazaki, Y., Bronkalla, O., & Morschhauser, A. (2021). The geomagnetic *Kp* index and derived indices of geomagnetic activity. *Space Weather*, 19, e2020SW002641. https://doi.org/10.1029/2020SW002641

Maruyama, N., Sun, Y., Richards, P. G., Middlecoff, J., Fang, T., Fuller-Rowell, T. J., et al. (2016). A new source of the midlatitude ionospheric peak density structure revealed by a new ionosphere-plasmasphere model. *Geophysical Research Letters*, **43**(6), 2429–2435. https://doi.org/10.1002/2015GL067312

Oliveira, D. M., & Zesta, E. (2019). Satellite orbital drag during magnetic storms. *Space Weather*, 17, 1510–1533. https://doi.org/10.1029/2019SW002287

Oliveira, D. M., Zesta, E., & Garcia-Sage, K. (2025). Tracking Reentries of Starlink Satellites During the Rising Phase of Solar Cycle 25. Frontiers in Astronomy and Space Sciences, 12. https://doi.org/10.3389/fspas.2025.1572313

Parker, W. E., & Linares, R. (2026). Data-driven satellite drag modeling without dynamic knowledge of the atmosphere. *Space Weather*, 24, e2025SW004729. https://doi.org/10.1029/2025SW004729

Picone, J. M., Hedin, A. E., Drob, D. P., & Aikin, A. C. (2002). NRLMSISE-00 empirical model of the atmosphere: Statistical comparisons and scientific issues. *Journal of Geophysical Research*, **107**(A12). SIA 15-1–SIA 15-16. https://doi.org/10.1029/2002JA009430

Ridley, A., Y. Deng, and G. Toth (2006), The global ionosphere—Thermosphere model, *J. Atmos. Sol. Terr. Phys.*, **68**(8), 839–864, doi:10.1016/j.jastp.2006.01.008.

Rostoker, G. (1972), Geomagnetic indices, *Rev. Geophys.*, 10(4), 935–950, doi:10.1029/RG010i004p00935.

Storz, M. F., Bowman, B. R., Branson, M. J. I., Casali, S. J., & Tobiska, W. K. (2005). High accuracy satellite drag model (HASDM). *Advances in Space Research*, **36**(12), 2497–2505. https://doi.org/10.1016/j.asr.2004.02.020

Thayer, J.P., Tobiska, W.K., Pilinski, M.D. and Sutton, E.K. (2021). Remaining Issues in Upper Atmosphere Satellite Drag. In Space Weather Effects and Applications (eds A.J. Coster, P.J. Erickson, L.J. Lanzerotti, Y. Zhang and L.J. Paxton). https://doi.org/10.1002/9781119815570.ch5

Vallado, D. A., Crawford, P., Hujsak, R., & Kelso, T. S. (2006). Revisiting Spacetrack Report #3. *AIAA/AAS Astrodynamics Specialist Conference*, Keystone, CO. AIAA 2006-6753. https://doi.org/10.2514/6.2006-6753

Wang, J. C., Yue, J., Bruinsma, S., Kuznetsova, M., Sypal, J., Mullinix, R., et al. (2026). Comprehensive and open assessment of thermospheric models during geomagnetic storm times within CCMC framework. *Space Weather*, 24, e2025SW004782. https://doi.org/10.1029/2025SW004782

Zesta, E., & Oliveira, D. M. (2019). Thermospheric heating and cooling times during geomagnetic storms, including extreme events. *Geophysical Research Letters*, 46, 12739–12746. https://doi.org/10.1029/2019GL085120